


**Microscopic Imaging Homogeneous and Single Phase Superfluid Density in  $\text{UTe}_2$** Yusuke Iguchi<sup>1,2</sup>, Huiyuan Man<sup>1,3</sup>, S. M. Thomas<sup>4</sup>, Filip Ronning<sup>4</sup>, Priscila F. S. Rosa<sup>4</sup>, and Kathryn A. Moler<sup>1,2,5</sup><sup>1</sup>*Geballe Laboratory for Advanced Materials, Stanford University, Stanford, California 94305, USA*<sup>2</sup>*Stanford Institute for Materials and Energy Sciences, SLAC National Accelerator Laboratory, 2575 Sand Hill Road, Menlo Park, California 94025, USA*<sup>3</sup>*Stanford Nano Shared Facilities, Stanford University, Stanford, California 94305, USA*<sup>4</sup>*Los Alamos National Laboratory, Los Alamos, New Mexico 87545, USA*<sup>5</sup>*Department of Applied Physics, Stanford University, Stanford, California 94305, USA* (Received 17 October 2022; revised 21 December 2022; accepted 4 April 2023; published 12 May 2023)

Odd-parity superconductor  $\text{UTe}_2$  shows spontaneous time-reversal symmetry breaking and multiple superconducting phases, which imply chiral superconductivity, but only in a subset of samples. Here we microscopically observe a homogeneous superfluid density  $n_s$  on the surface of  $\text{UTe}_2$  and an enhanced superconducting transition temperature near the edges. We also detect vortex-antivortex pairs even at zero magnetic field, indicating the existence of a hidden internal field. The temperature dependence of  $n_s$ , determined independent of sample geometry, does not support point nodes along the  $b$  axis for a quasi-2D Fermi surface and provides no evidence for multiple phase transitions in  $\text{UTe}_2$ .

DOI: [10.1103/PhysRevLett.130.196003](https://doi.org/10.1103/PhysRevLett.130.196003)

Strong spin-orbit coupled unconventional superconductors, whose superconducting (SC) state cannot be described by electron-phonon coupling, provide a platform for experimental and theoretical studies of emergent quantum behavior [1,2]. Time reversal and parity are key symmetries to characterize these materials, and striking states of matter often emerge when one (or both) of these symmetries are broken. For instance, odd-parity superconductors have been identified as a promising route for topological superconductivity, which hosts edge modes or vortices with non-Abelian statistics required for topological quantum computing [3]. A chiral superconductor further breaks time-reversal symmetry and may lower the energy of the SC condensate by removing nodes from the gap function [4]. Odd-parity chiral superconductors are remarkably rare, but their experimental manifestation has been observed in superfluid  $^3\text{He}$  and actinide superconductor  $\text{UPT}_3$  [5].

$\text{UTe}_2$  is a newly discovered candidate for odd-parity chiral superconductivity [6,7]. Nuclear magnetic resonance (NMR) Knight shift measurements strongly suggest that  $\text{UTe}_2$  is an odd-parity superconductor with a dominant  $B_{3u}$  order parameter [8–10]. Point nodes in the SC gap structure are supported by thermal transport and specific heat measurements [6,11,12], Knight shift measurements [10], and nonlocal superfluid density measurements [13]. The position of the point nodes, however, is still controversial. Thermal conductivity, microwave surface impedance, and specific heat measurements suggest point nodes in the  $ab$  plane or along  $a$  [11–13], whereas magnetic penetration depth measurements argue for a multicomponent SC state with multiple point nodes near the  $b$  and  $c$  axes [14].

Evidence for chiral superconductivity was found in  $\text{UTe}_2$  by scanning tunneling spectroscopy on the step edges of a

( $0\bar{1}1$ ) plane [15] and by polar Kerr rotation measurements [16]. Multiple SC phase transitions were also reported in  $\text{UTe}_2$  even at ambient pressure at zero magnetic field by specific heat measurements [16,17]. Subsequently, it was found that the observed “double peak” in the specific heat can arise from sample inhomogeneity [7,18]. In addition, a single phase transition is reported in higher-quality samples with higher SC critical temperature  $T_c$ , higher residual resistivity ratios, and lower residual resistivities in  $\text{UTe}_2$  crystals grown using the chemical vapor transport [19] and quantum oscillations in salt-flux-grown crystals [20–22]. To microscopically investigate the SC state of  $\text{UTe}_2$ , here we report the temperature dependence of the local superfluid response using scanning superconducting quantum interference device (SQUID) susceptometry on a cleaved (011) plane of  $\text{UTe}_2$ . We also image the pinned vortices induced by field cooling. Our results show no evidence for multiple phase transitions in the temperature dependence of the superfluid density and imply an anisotropic nodal gap structure in  $\text{UTe}_2$ .

Bulk single crystals of  $\text{UTe}_2$  were grown by chemical vapor transport. Samples nos. 1 and 2 used in this Letter were obtained from the same batch as sample s2 in Ref. [19] because high enough quality samples are necessary for our local measurements to obtain the superfluid density at a homogeneous area within the penetration depth. Heat capacity measurements confirmed a single SC transition at  $T_c = 1.68$  K with a width of 50 mK on a single crystal, which was subsequently cleaved into two samples used in this study. We used a scanning SQUID susceptometer to obtain the local ac susceptibility on a cleaved (011) plane of  $\text{UTe}_2$  at temperatures from 80 mK to

2 K in a Bluefors LD dilution refrigerator. Our scanning SQUID susceptometer has two pickup loop and field coil pairs configured with a gradiometric structure [23]. The inner radius of the pickup loop is  $0.4\ \mu\text{m}$  and the inner radius of the field coil is  $1.5\ \mu\text{m}$ . The scan height is  $\sim 500\ \text{nm}$ . The pickup loop provides the local dc magnetic flux  $\Phi$  in units of the flux quantum  $\Phi_0 = h/2e$ , where  $h$  is the Planck constant and  $e$  is the elementary charge. The pickup loop also detects the ac magnetic flux  $\Phi^{\text{ac}}$  in response to an ac magnetic field  $He^{i\omega t}$ , which was produced by an ac current of  $|I^{\text{ac}}| = 1\ \text{mA}$  at a frequency  $\omega/2\pi \sim 1\ \text{kHz}$  through the field coil, using an SR830 lock-in amplifier. Here we report the local ac susceptibility as  $\chi = \Phi^{\text{ac}}/|I^{\text{ac}}|$  in units of  $\Phi_0/A$ .

To obtain the homogeneity of the superfluid density and its local temperature dependence, we measured the local susceptibility near the edge of the sample [Figs. 1(a)–1(e)]. The susceptibility far from the edge has a homogeneous temperature dependence on the micron scale [Fig. 1(f)]. We note that our results do not rule out possible inhomogeneity either on the nanoscale or on scales larger than the scan area (e.g., submillimeter). Our data also cannot rule out fluctuations in time. There is no kink in the temperature dependence of the local susceptibility below  $T_c$ , wherein the temperature step of the scans is 25 mK. The susceptibility is positive above  $T_c$  due to paramagnetism. The local susceptibility was negative (diamagnetic) near the edge but positive far from the edge at 1.69 K [Figs. 1(c) and 1(f)].

We defined the local  $T_c$  as the temperature that satisfies the relation of  $\chi(T > T_c) > -0.1\ \Phi_0/A$ . The local  $T_c$  mapping clearly shows that the local  $T_c$  is weakly enhanced from 1.68 to 1.71 K at the edge, but is homogeneous 30  $\mu\text{m}$  away from the edge into the sample (Fig. 2, sample no. 1; Fig. S2, in the Supplemental Material [24] sample no. 2). We note that the amplitude of the susceptibility near the edge within the penetration depth in Fig. 1(f) is lower than the actual value because the penetration depth is longer than the pickup loop's scale and the susceptibility loses some signal at the edge. This artificial effect explains the

downward curve of local  $T_c$  at the right side of the peak and also may cause a possible lower estimate of local  $T_c$  near the edge in Fig. 2, where we plot all pixels of  $T_c < 1.67\ \text{K}$  with black colors. If two phase transitions do exist, they must be closer to each other than 25 mK, or the second kink below  $T_c$  is much smaller than our experimental noise.

Now we turn to the pinned vortex density, which reflects the impurity density on the crystal surface for small applied magnetic fields. The distance between vortices is on the order of microns. Our magnetometry scan imaged the pinned vortices induced by cooling in an applied uniform magnetic field normal to the scan surface from 2 K to 100 mK [Figs. 3(a) and 3(b), sample no. 1; Figs. S3(a) and S3(b) [24], sample no. 2]. The number of vortices corresponds to the applied field, but the vortices are preferentially pinned along lines in one direction, which is parallel to the sample edge. This linear alignment of pinned vortices indicates the existence of a line anomaly, such as nanometer-scale step edges along crystal axes. Near zero magnetic field, there are still a few vortices and antivortices pinned far from the edge [Fig. 3(c), sample no. 1; Fig. S3(c) [24], sample no. 2]. Notably, these vortices and antivortices do not disappear after zero field cooling with slower cooling rates, which is expected to cancel the uniform background field normal to the sample surface by the application of an external field. These data are inconsistent with the argument from polar Kerr effect measurements that there are no vortices in  $\text{UTe}_2$  within the beam size area ( $\sim 11\ \mu\text{m}$  radius) [25]. To precisely analyze the relation between the vortex density and the external field, we plot the field amplitude estimated from the vortex or antivortex density after field cooling and the external field estimated using the Biot-Savart law as a function of the applied current in the magnetic field coil used in field cooling in Fig. 3(e). By taking the difference between the field trapped in vortices  $H_v = N_v \Phi_0/S$ , where  $N_v$  is the number of vortices and  $S$  is the scan area, and the external field  $H_{\text{BG}}$ , we obtain a small ferromagneticlike field dependence [Fig. 3(f)]. This field dependence implies the existence of a hidden internal field that can be reversed by

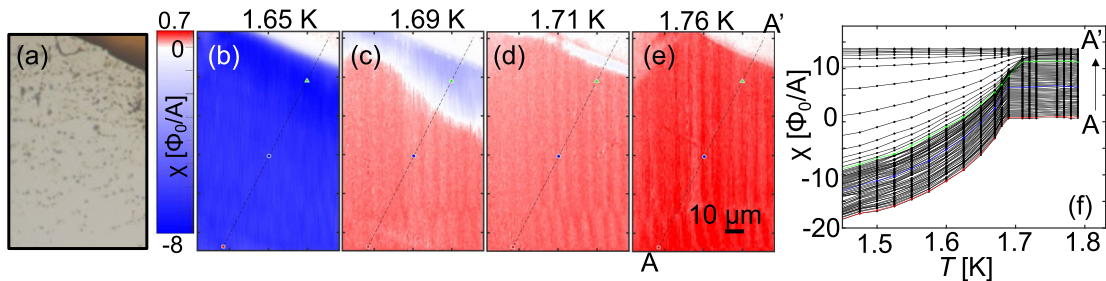


FIG. 1. Local susceptibility is microscopically homogeneous on (011) surface of  $\text{UTe}_2$  sample no. 1. (a) Optical image of the scanned area, which includes the cleaved (011) surface with small bumps creating no signals in our scans and the edge. (b)–(e) Temperature dependence of the susceptometry scan indicates the homogeneous superfluid density on  $\text{UTe}_2$ . Stripes along the scan directions are the scanning noise. (f) The temperature dependence of the local susceptibility at the points from A to A' in Fig. 1(e) has no kink below  $T_c$ . The susceptibilities are shifted by  $0.2\ \Phi_0/A$  for clarity except for the data at A.

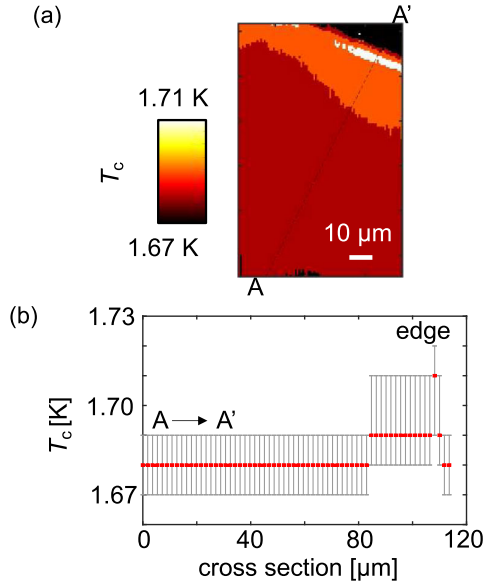


FIG. 2. Small enhancement of local  $T_c$  near the edge of sample no. 1. (a) The local  $T_c$  mapping is obtained from the local susceptometry scans. (b) Cross section of the local  $T_c$  from  $A$  to  $A'$  shows the local  $T_c$  enhancement of 30 mK at the edge. The error bars are obtained as the minimum size of temperature steps of scans. The plotted area and the cross section from  $A$  to  $A'$  are the same as Fig. 1.

$H_{BG} > 0.1$  Oe. The saturated amplitude of the hidden magnetic moments is estimated as 0.01–0.02 G, which is in the same order as the upper limit of the possible internal field estimated by previous bulk SQUID magnetometry measurements [26]. Further, our results indicate the existence of a local magnetic source, which is likely sample dependent, that induces vortices and antivortices, in spite of the absence of long-range order or strong magnetic sources on the scan plane above  $T_c$  [6,27,28]. Small dipole fields are observed at the edge of the sample, which may stem from U impurities; however, these impurities cannot induce pinned vortices and antivortices as they are too far away [Fig. 3(d), sample no. 1]. Muon spin resonance and NMR measurements have detected the presence of strong and slow magnetic fluctuations in  $UTe_2$  at low temperatures [29,30]. Therefore, a sensible scenario is that these fluctuations are pinned by defects and become locally static.

To estimate the local superfluid density, we measure the local susceptibility at different temperatures with the pickup loop position fixed. The local superfluid density is obtained using the numerical expression of the susceptibility assuming a homogeneous penetration depth  $\lambda$ , as described below. Kirtley *et al.* developed the expression for the susceptibility as a function of the distance between the susceptometer and the sample surface [31]. In this model, wherein the sample surface is at  $z = 0$ , we consider three

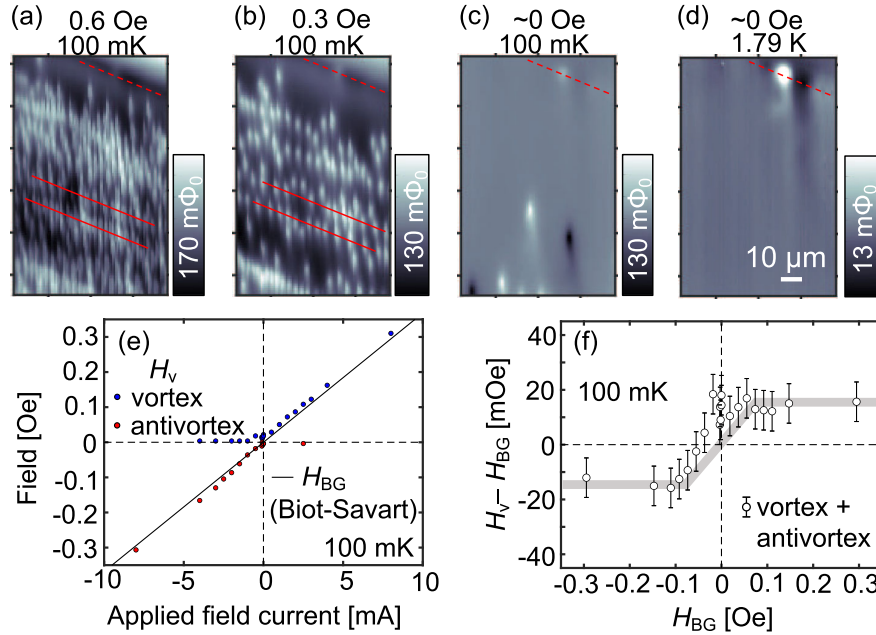


FIG. 3. The vortex density is homogeneous over many-micron distances. The existence of vortices and antivortices in low-field scans may indicate a local magnetic source in sample no. 1. (a),(b) Local magnetometry scan after field cooling shows the vortices pinned parallel to the sample edge, as denoted by the dashed lines. (c) There are a few vortices and antivortices pinned far from the edge after near zero field cooling. (d) Magnetometry scan near zero field above  $T_c$  shows a small magnetic dipole at the sample's edge, but no other indication of magnetism. The “tail” of the vortices and dipoles are due to the asymmetric shielding structure of the scanning SQUID [23]. (e) There is a small gap between the field estimated from the field-cooled vortex density and the applied field. (f) At  $|H_{BG}| > \sim 0.1$  Oe, the gap  $H_v - H_{BG}$  is saturated and either vortices or antivortices are dominantly pinned. The uncertainty due to the error in counting vortices is  $\pm 1\Phi_0$ . The thick gray line is a guide to the eye.

regions. Above the sample ( $z > 0$ ), the pickup loop and field coil are at  $z$  in vacuum and  $\mu_1 = \mu_0$ , where  $\mu_0$  is the permeability in vacuum. In the sample ( $-t \leq z \leq 0$ ), the London penetration depth is  $\lambda = \sqrt{m/4\pi ne^2}$ , and the permeability is  $\mu_2$ , where  $t$  is the sample thickness. Below the sample ( $z < -t$ ), there is a nonsuperconducting

substrate with a permeability  $\mu_3$ . The radius of the field coil and the pickup loop are  $a$  and  $b$ , respectively. By solving Maxwell's equations and the London equation for the three regions in the limit of  $b \ll a$ , the SQUID height dependence of the susceptibility  $\chi(z)$  is expressed as

$$\chi(z)/\phi_s = \int_0^\infty dx e^{-2x\bar{z}} x J_1(x) \left[ \frac{-(\bar{q} + \bar{\mu}_2 x)(\bar{\mu}_3 \bar{q} - \bar{\mu}_2 x) + e^{2\bar{q}\bar{t}}(\bar{q} - \bar{\mu}_2 x)(\bar{\mu}_3 \bar{q} + \bar{\mu}_2 x)}{-(\bar{q} - \bar{\mu}_2 x)(\bar{\mu}_3 \bar{q} - \bar{\mu}_2 x) + e^{2\bar{q}\bar{t}}(\bar{q} + \bar{\mu}_2 x)(\bar{\mu}_3 \bar{q} + \bar{\mu}_2 x)} \right], \quad (1)$$

where  $\phi_s = A\mu_0/2\Phi_0 a$  is the self inductance between the field coil and the pickup loop,  $A$  is the effective area of the pickup loop,  $\bar{z} = z/a$ ,  $J_1$  is the Bessel function of first order,  $\bar{\mu}_2 \equiv \mu_2/\mu_0$ ,  $\bar{t} = t/a$ ,  $\bar{q} = \sqrt{x^2 + \bar{\lambda}^{-2}}$ , and  $\bar{\lambda} = \lambda/a$ . For the bulk sample on a copper substrate ( $\bar{t} \gg 1$ ,  $\bar{\mu}_3 = 1$ ), the observed susceptibility only depends on  $\lambda$ ,  $\mu_2$ , and the SQUID structure.

The penetration depth  $\lambda(T)$  was calculated using Eq. (1) and the observed susceptibility [Fig. 4(a)]. The normalized superfluid density  $n_s = \lambda^2(0)/\lambda^2(T)$  was calculated from the obtained penetration depth's temperature dependence, where  $\lambda(0) = 1620 \pm 150$  nm (sample no. 1) and  $1730 \pm 300$  nm (sample no. 2) [Fig. 4(b)]. Here the error for  $\lambda$  and  $n_s$  is roughly calculated from the pickup loop height uncertainty. We note that sample no. 2 had a dead layer of 700 nm on the surface, which we estimated by assuming

that sample no. 2 has a similar penetration depth at zero temperature with sample no. 1, because sample no. 2 was accidentally exposed in air about one extra hour. The locally obtained superfluid density  $n_s$  saturates below  $T/T_c = 0.1$ .

We examine the SC gap structure through the temperature dependence of the superfluid density. The superfluid density  $n_i = [\lambda_i(0)/\lambda_i(T)]^2$  is sensitive to low-energy excitations along the  $i$  axis, which is perpendicular to the applied field. The penetration depth  $\lambda_i(T)$  is defined by the London equation,  $j_{si} = (-1/\mu_0 \lambda_i^2) A_i$ , where  $j_{si}$  is the  $i$  component of the supercurrent density and  $A_i$  is the  $i$  component of the vector potential [24,32]. In our case, the measured superfluid density is sensitive to excitations within the plane normal to [011] with the applied ac field along [011] and expressed by  $n_{(011)} \equiv (n_a + n_{\perp[011],a})/2$ ,

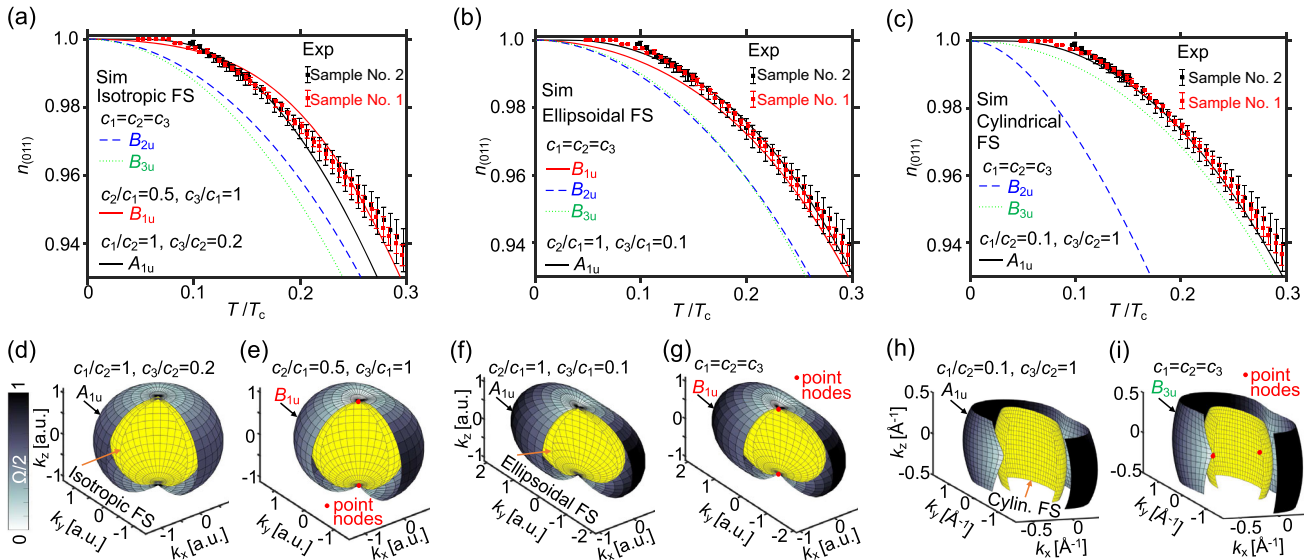


FIG. 4. The temperature dependence of the superfluid density best matches an anisotropic, rather than isotropic, gap structure. (a)–(c) Temperature dependence of the normalized superfluid density  $n_{(011)}$  at the fixed position in sample no. 1 and no. 2 that are indicated by the blue dot in Figs. 1(b) and S1(b) [24], respectively. The thick lines are simulation curves best fit for four gap symmetries with (a) isotropic FS, (b) ellipsoidal FS, and (c) cylindrical FS (see Supplemental Material [24]). (d)–(i) Best fit models of gap symmetries (d),(e), (f),(g) and (h),(i) for (a), (b), and (c), respectively. FS is plotted by yellow color. The distance between larger surfaces and FS represents the angular dependence of the SC gap  $\Omega$  in (a),(b) the spherical coordinate and (c) the cylindrical coordinate. All surfaces are cut for clarity.

where  $n_{\perp[011],a} \equiv n_j$  with the  $j$  direction normal to the [011] direction and the  $a$  axis. The SC gap function of  $\text{UTe}_2$   $\Delta$  is most likely odd parity within the orthorhombic  $D_{2h}$  point group. In the presence of strong spin-orbit coupling,  $\Delta(T, \vec{k}) = \Psi(T)\Omega(\vec{k})$ , and the angle dependence of the gap function is expressed as  $\Omega(\vec{k}) \propto \sqrt{\vec{d} \cdot \vec{d}^* \pm |i\vec{d} \times \vec{d}^*|}$ . In this case, the possible irreducible representations are  $A_{1u}$  [full gap,  $\vec{d} = (c_1k_x, c_2k_y, c_3k_z)$ ],  $B_{1u}$  [point nodes along  $c$ ,  $\vec{d} = (c_1k_y, c_2k_x, c_3k_xk_yk_z)$ ],  $B_{2u}$  [point nodes along  $b$ ,  $\vec{d} = (c_1k_z, c_2k_xk_yk_z, c_3k_x)$ ], and  $B_{3u}$  [point nodes along  $a$ ,  $\vec{d} = (c_1k_xk_yk_z, c_2k_z, c_3k_y)$ ] [33]. We note that coefficients  $c_1$ ,  $c_2$ , and  $c_3$  may differ by orders of magnitude [34].

For the sake of completeness, here we assume three cases of Fermi surface structure to calculate the temperature-dependent superfluid density with fit parameters  $c_1$ ,  $c_2$ , and  $c_3$  [24,35]: (I) isotropic Fermi surface (FS) based on the isotropic heavy 3D Fermi surface observed by angle-resolved photoemission spectroscopy (ARPES) measurements [36,37], (II) ellipsoidal FS based on the upper critical field [38], and (III) cylindrical FS. Case (III) is based on both ARPES measurements, which observed cylindrical light electron bands [36,37] and recent de Haas–van Alphen measurements that reveal heavy cylindrical bands [21].

The isotropic fully gapped model  $A_{1u}$  saturates at  $T/T_c = 0.2$  (Fig. S6 [24]). In contrast, the experimental data saturate at a lower temperature, which implies an anisotropic structure in the SC gap function. The calculated normalized superfluid density  $n_{(011)}$  for highly anisotropic  $A_{1u}$  and  $B_{1u}$  have a similar temperature dependence compared to our experimental results, whereas  $n_{(011)}$  for  $B_{2u}$  and  $B_{3u}$  do not agree with our data because of their point nodes near the (011) plane with isotropic or ellipsoidal 3D Fermi surfaces [Figs. 4(a) and 4(b)]. For highly anisotropic  $A_{1u}$  and  $B_{3u}$ ,  $n_{(011)}$  agrees with our experimental results, whereas  $n_{(011)}$  for  $B_{2u}$  is inconsistent with the data for a cylindrical Fermi surface [Fig. 4(c)]. We note that our calculations with point nodes do not completely explain our results near zero temperature, which may be caused by our assumptions of the simplest structures of Fermi surface and gap functions, the simple averaging of  $n_a$  and  $n_{\perp[011],a}$ , or by the assumption of a single band. Our results indicate the existence of point nodes along the  $a$  axis for a cylindrical Fermi surface including  $B_{3u}$ , which is consistent with the microwave surface impedance measurements [13], and the multicomponent order  $B_{3u} + i\epsilon A_{1u}$  with a sufficiently small  $\epsilon$ . Our results are inconsistent with the existence of point nodes along the  $b$  axis, including the multicomponent order  $B_{3u} + iA_{1u}$  suggested by the tunneling diode measurements [14]. An anisotropic fully gapped component with deep minima is also allowed.

In summary, we microscopically imaged the superfluid density and the vortex density in high-quality samples of  $\text{UTe}_2$ . The superfluid density is homogeneous, and the

temperature dependence below the SC transition  $T_c$  does not show evidence for a second phase transition. The observed temperature dependence of the superfluid density can be explained by a  $B_{1u}$  order parameter for a 3D ellipsoidal (or isotropic) Fermi surface or by a  $B_{3u}$  order parameter for a quasi-2D cylindrical Fermi surface. A highly anisotropic  $A_{1u}$  symmetry component is also allowed for any Fermi surface structures. We conclude that our results are consistent with these combinations of gap symmetry. In light of our results, evidence for time-reversal symmetry breaking and chiral superconductivity in  $\text{UTe}_2$  could be understood either through the presence of vortices and antivortices even at zero applied field or by the presence of a finite anisotropic  $A_{1u}$  symmetry in the SC order parameter.

The authors thank J. Ishizuka for fruitful discussions. This work was primarily supported by the Department of Energy, Office of Science, Basic Energy Sciences, Materials Sciences and Engineering Division, under Award No. DE-AC02-76SF00515. Sample synthesis at L. A. N. L. was supported by the U.S. Department of Energy, Office of Basic Energy Sciences, Division of Materials Science and Engineering “Quantum Fluctuations in Narrow-Band Systems” project, while heat capacity measurements were performed with support from the LANL LDRD program. Y.I. was partially supported by the Japan Society for the Promotion of Science (JSPS), Overseas Research Fellowship.

- 
- [1] C. Pfleiderer, *Rev. Mod. Phys.* **81**, 1551 (2009).
  - [2] M. Smidman, M. B. Salamon, H. Q. Yuan, and D. F. Agterberg, *Rep. Prog. Phys.* **80**, 036501 (2017).
  - [3] M. Sato and Y. Ando, *Rep. Prog. Phys.* **80**, 076501 (2017).
  - [4] C. Kallin and J. Berlinsky, *Rep. Prog. Phys.* **79**, 054502 (2016).
  - [5] K. E. Avers, W. J. Gannon, S. J. Kuhn *et al.*, *Nat. Phys.* **16**, 531 (2020).
  - [6] S. Ran *et al.*, *Science* **365**, 684 (2019).
  - [7] D. Aoki, J.-P. Brison, J. Flouquet, K. Ishida, G. Knebel, Y. Tokunaga, and Y. Yanase, *J. Phys. Condens. Matter* **34**, 243002 (2022).
  - [8] G. Nakamine *et al.*, *J. Phys. Soc. Jpn.* **88**, 113703 (2019).
  - [9] G. Nakamine *et al.*, *Phys. Rev. B* **103**, L100503 (2021).
  - [10] H. Fujibayashi *et al.*, *J. Phys. Soc. Jpn.* **91**, 043705 (2022).
  - [11] T. Metz, S. Bae, S. Ran, I. Lin Liu, Y. S. Eo, W. T. Fuhrman, D. F. Agterberg, S. M. Anlage, N. P. Butch, and J. Paglione, *Phys. Rev. B* **100**, 220504(R) (2019).
  - [12] S. Kittaka, Y. Shimizu, T. Sakakibara, A. Nakamura, D. Li, Y. Homma, F. Honda, D. Aoki, and K. Machida, *Phys. Rev. Res.* **2**, 032014(R) (2020).
  - [13] S. Bae, H. Kim, Y. S. Eo, S. Ran, I.-I. Liu, W. T. Fuhrman, J. Paglione, N. P. Butch, and S. M. Anlage, *Nat. Commun.* **12**, 2644 (2021).
  - [14] K. Ishihara, M. Roppongi, M. Kobayashi, Y. Mizukami, H. Sakai, Y. Haga, K. Hashimoto, and T. Shibauchi, [arXiv: 2105.13721](https://arxiv.org/abs/2105.13721).

- [15] L. Jiao, S. Howard, S. Ran, Z. Wang, J. O. Rodriguez, M. Sigrist, Z. Wang, N. P. Butch, and V. Madhavan, *Nature (London)* **579**, 523 (2020).
- [16] I. M. Hayes *et al.*, *Science* **373**, 797 (2021).
- [17] S. M. Thomas, F. B. Santos, M. H. Christensen, T. Asaba, F. Ronning, J. D. Thompson, E. D. Bauer, R. M. Fernandes, G. Fabbris, and P. F. S. Rosa, *Sci. Adv.* **6**, eabc8709 (2020).
- [18] S. M. Thomas, C. Stevens, F. B. Santos, S. S. Fender, E. D. Bauer, F. Ronning, J. D. Thompson, A. Huxley, and P. F. S. Rosa, *Phys. Rev. B* **104**, 224501 (2021).
- [19] P. F. S. Rosa, A. Weiland, S. S. Fender, B. L. Scott, F. Ronning, J. D. Thompson, E. D. Bauer, and S. M. Thomas, *Commun. Mater.* **3**, 33 (2022).
- [20] H. Sakai, P. Opletal, Y. Tokiwa, E. Yamamoto, Y. Tokunaga, S. Kambe, and Y. Haga, *Phys. Rev. Mater.* **6**, 073401 (2022).
- [21] D. Aoki *et al.*, *J. Phys. Soc. Jpn.* **91**, 083704 (2022).
- [22] A. G. Eaton *et al.*, [arXiv:2302.04758](https://arxiv.org/abs/2302.04758).
- [23] J. R. Kirtley *et al.*, *Rev. Sci. Instrum.* **87**, 093702 (2016).
- [24] See Supplemental Material at <http://link.aps.org/supplemental/10.1103/PhysRevLett.130.196003> for the details of anisotropic superfluid density calculations and experimental data of magnetometry and susceptometry on sample no. 2.
- [25] D. S. Wei, D. Saykin, O. Y. Miller, S. Ran, S. R. Saha, D. F. Agterberg, J. Schmalian, N. P. Butch, J. Paglione, and A. Kapitulnik, *Phys. Rev. B* **105**, 024521 (2022).
- [26] C. Paulsen, G. Knebel, G. Lapertot, D. Braithwaite, A. Pourret, D. Aoki, F. Hardy, J. Flouquet, and J.-P. Brison, *Phys. Rev. B* **103**, L180501 (2021).
- [27] A. Miyake, Y. Shimizu, Y. J. Sato, D. Li, A. Nakamura, Y. Homma, F. Honda, J. Flouquet, M. Tokunaga, and D. Aoki, *J. Phys. Soc. Jpn.* **88**, 063706 (2019).
- [28] V. Hutanu, H. Deng, S. Ran, W. T. Fuhrman, H. Thomad, and N. P. Butch, *Acta Cryst. B* **76**, 137 (2020).
- [29] Y. Tokunaga *et al.*, *J. Phys. Soc. Jpn.* **91**, 023707 (2022).
- [30] S. Sundar *et al.*, *Commun. Phys.* **6**, 24 (2023).
- [31] J. R. Kirtley *et al.*, *Phys. Rev. B* **85**, 224518 (2012).
- [32] B. S. Chandrasekhar and D. Einzel, *Ann. Phys. (N.Y.)* **2** (new volume **505**), 535 (1993).
- [33] J. F. Annett, *Adv. Phys.* **39**, 83 (1990).
- [34] J. Ishizuka and Y. Yanase, *Phys. Rev. B* **103**, 094504 (2021).
- [35] V. G. Kogan and R. Prozorov, *Phys. Rev. B* **103**, 054502 (2021).
- [36] S.-I. Fujimori, I. Kawasaki, Y. Takeda, H. Yamagami, A. Nakamura, Y. Homma, and D. Aoki, *J. Phys. Soc. Jpn.* **88**, 103701 (2019).
- [37] L. Miao *et al.*, *Phys. Rev. Lett.* **124**, 076401 (2020).
- [38] D. Aoki *et al.*, *J. Phys. Soc. Jpn.* **88**, 043702 (2019).